Hybrid density functional study of structural, bonding, and electronic properties of the manganite series La$_{1-x}$Ca$_x$MnO$_3$ ($x = 0, \frac{1}{4}, 1$)

R. Korotana,[1,*] G. Mallia,[1] Z. Gercsi,[2] L. Liborio,[1] and N. M. Harrison[1,3]

[1]*Thomas Young Centre, Department of Chemistry, Imperial College London, South Kensington, London SW7 2AZ, United Kingdom*

[2]*Blackett Laboratory, Department of Physics, Imperial College London, South Kensington, London SW7 2AZ, United Kingdom*

[3]*STFC Daresbury Laboratory, Daresbury, Warrington WA4 4AD, United Kingdom*

Hybrid-exchange density functional theory calculations are carried out to determine the effects of A-site doping on the electronic and magnetic properties of the manganite series La$_{1-x}$Ca$_x$MnO$_3$. This study focuses on the ground state of an ordered Ca occupancy in a periodic structure. It is shown that the hybrid-exchange functional, Becke three-parameter Lee-Yang-Parr (B3LYP), provides an accurate and consistent description of the electronic structure for LaMnO$_3$, CaMnO$_3$, and La$_{0.75}$Ca$_{0.25}$MnO$_3$. We have quantified the relevant structural, magnetic, and electronic energy contributions to the stability of the doped compound. An insight into the exchange coupling mechanism for the low hole density region of the phase diagram, where a polaron (anti-Jahn-Teller) forms, is also provided. This study completes a microscopic description of the lightly doped insulator with an antiferromagnetic-to-ferromagnetic and metal-to-insulator transition.

I. INTRODUCTION

Since the discovery of the metal-insulator transition in manganites over 50 years ago [1], great efforts have been devoted to understanding their properties. Manganites with a general formula $R_{(1-x)}A_x$MnO$_3$ (R being rare earth and A earth alkaline elements) are perovskite structured oxides, which display a range of interesting phenomena, such as high-temperature superconductivity [2,3], colossal magnetoresistance (CMR) [4–6], and the magnetocaloric effect (MCE) [7–9]. Such properties are strongly dependent on the doping concentration x as well as on external variables, such as temperature, pressure, and electric and/or magnetic fields. The rich diversity in crystallographic, magnetic, and electronic phases [10–12] displayed by manganites is primarily attributed to a strong interplay between spin, charge, orbital, and lattice degrees of freedom. As a consequence of the effects of strong electron correlation, a complete microscopic understanding of the physics underlying the properties of manganites has not yet been achieved.

Experimental studies on manganites doped with divalent earth alkaline elements, such as Ca, Ba, and Sr, have been the subject of intense study since the discovery of CMR [6,13]. In particular, the La$_{1-x}$Ca$_x$MnO$_3$ series undergoes a phase transition from a low-temperature ferromagnetic metallic (FM-M) to a high-temperature paramagnetic insulating (PM-I) phase for $0.2 < x < 0.5$ [14]. The crystal structure below the Curie temperature T_C for the FM-M phase is orthorhombic [15,16]. The T_C has been obtained experimentally from the temperature dependence of the resistivity (using the four-probe method [17–21]) and magnetization measurements (using a superconducting quantum interference device [13,18,19,21–23] and the vibrating sample magnetometer [17,20,24,25]). It depends strongly on x and also the preparation conditions (and resultant crystallinity) of the samples. When considering the $0.2 < x < 0.5$ doping range, T_C at $x = 0.2$ has been found

to be 176 K [9,15] and 230 K [9,24] for single crystal and polycrystalline samples, respectively, while at $x = 0.45$ for a polycrystalline sample, T_C is 238 K [9,24]. The $x = 1/3$ composition has received considerable attention, because for this material T_C is maximized with a value in the range 252–267 K [9,24].

Early attempts to explain the electronic structure and magnetic properties of mixed-valency manganites were made by Zener [26,27], who proposed that the low-temperature FM-M phase for the La$_{1-x}$Ca$_x$MnO$_3$ series is attributed to the double-exchange (DE) mechanism. Zener's DE model involves spin coupling between Mn^{3+} and Mn^{4+} next-nearest-neighbor ions with the conduction electrons mediating the interaction. However, the DE model yields a T_C higher, by an order of magnitude, than that determined experimentally [5,28]. It has been proposed [28,29] that this discrepancy is due to the neglect of electron-lattice interactions in the DE model. The effective Debye-Waller factors of Mn-O pairs and the pair distribution function of local bond lengths [determined experimentally using extended x-ray fine absorption structure (EXAFS) and neutron powder-diffraction data] indicate distortions of the MnO$_6$ octahedron [30–34]. Such experiments support the view that strong hole-lattice coupling is important. Understanding the transition from a low-temperature, metallic, magnetically ordered regime to a high-temperature, polaron-dominated, and magnetically disordered regime requires a theory capable of describing the localized electronic state polaron and the strongly correlated metal. This is a major challenge for the theory of electronic structure in condensed matter.

When considering a single phase, the majority of quantum mechanical simulations performed on the La$_{1-x}$Ca$_x$MnO$_3$ manganite series have been for the $x = 1/2$ composition [18,35,36] and the parent, LaMnO$_3$ (see Ref. [37] and references therein for a systematic review). In particular, band calculations have been carried out within the local density approximation (LDA) of density functional theory (DFT). This approximation, however, fails to describe the LaMnO$_3$ insulating cubic phase, since it excessively delocalizes the

*romi.korotana09@imperial.ac.uk

electron density [38]. The LDA also underestimates the band gap for the orthorhombic phase [39] and a qualitatively correct description of the orbitally ordered ground state is difficult to obtain [40]. Further studies based on the generalized gradient approximation (GGA) of the exchange correlation fail to predict the correct magnetic ground state [41,42]. The band structure and insulating character of LaMnO$_3$ are described correctly through the use of the Hartree-Fock (HF) method in its spin polarized [unrestricted Hartree-Fock (UHF)] implementation [43–45]. However, the band gap is significantly overestimated due to the neglect of electron correlation. Moreover, physical properties such as the exchange constants are underestimated [44].

Other first principles studies [46,47], for the end members, have focused on the LDA+U method. This approach treats the on-site Coulomb interactions in a mean-field approximation using semiempirical parameters and has been implemented as a correction to the local spin density approximation (LSDA) [48,49]. Although this method significantly improves the description of the endpoint compounds, it is not ideal since the energetics are highly dependent on the choice of the U parameter. Therefore it is important to go beyond standard exchange-correlation potentials, which are limited in describing localized electronic states.

It is worth mentioning that very few first principles studies have been carried out to investigate other compositions in the La$_{1-x}$Ca$_x$MnO$_3$ series. The $x = 1/4$ and $x = 1/3$ compounds have been studied within the LSDA, for a simplified cubic perovskite structure [39], and the GGA without correction, for the orthorhombic perovskite structure [50]. However, a detailed electronic structure calculation, which provides an insight into the relevant energy scales that contribute to the stability of manganites, has not yet been carried out. In order to do so, one has to disentangle and quantify the competing interactions. In this paper, we analyze such energy contributions, as well as the effects of doping, concentrating mainly on the low-temperature ($T = 0$ K) properties and on the nature of the (meta)stable state(s) in an ordered Ca distribution model. The hybrid-exchange density functional, Becke three-parameter Lee-Yang-Parr (B3LYP), has been adopted, since transition metal oxide systems are characterized by a strong interplay between the electronic and geometrical structure. It is well documented that this functional provides a more qualitatively correct description of the electronic structure of localized and strongly correlated systems [45,51–60].

We present a theoretical investigation on the structural, electronic, and magnetic properties of the manganite series La$_{1-x}$Ca$_x$MnO$_3$, using hybrid-exchange DFT calculations. As a first step towards predicting the effects of doping, the ordered endpoint compounds have been studied as references for the doped composition. This provides a basis for validation of the theory and numerical approximations. The correlation between conductivity and magnetism is a fundamental feature of manganites. Therefore, the nearest-neighbor superexchange coupling constants have also been calculated by adopting the broken symmetry Kohn-Sham approach [61,62].

The paper is organized as follows: In Sec. II the computational details are provided and the results are presented in Sec. III. The discussion begins with the optimized geometries of the endpoint compounds, LaMnO$_3$ and CaMnO$_3$, followed by an analysis of the electronic structures. The focus of the discussion is the effect of Ca doping for $x = 1/4$ on the structural, magnetic, and electronic properties. Conclusions are drawn in Sec. IV.

II. COMPUTATIONAL DETAILS

All the calculations have been performed using CRYSTAL09 [63], a code based on the expansion of the crystalline orbitals as a linear combination of a local basis set (BS) consisting of atom centered Gaussian orbitals. The Mn, O, and Ca ions are described by a triple valence all-electron BS: an 86-411d(41) contraction (one s, four sp, and two d shells), an 8-411d(1) contraction (one s, three sp, and one d shells), and an 8-65111(21) contraction (one s, three sp, and two d shells), respectively; the most diffuse $sp(d)$ exponents are $\alpha^{Mn} = 0.4986(0.249)$, $\alpha^{O} = 0.1843(0.6)$, and $\alpha^{Ca} = 0.295(0.2891)$ bohr^{-2}. The La basis set includes a relativistic pseudopotential to describe the core electrons, while the valence part consists of a 411p(411)d(311) contraction scheme (with three s, three p, and three d shells); the most diffuse exponent is $\alpha^{La} = 0.15$ bohr^{-2} for each s, p, and d [45].

Electron exchange and correlation are approximated using the B3LYP hybrid-exchange functional, which, as noted

(a) LaMnO$_3$ (b) CaMnO$_3$

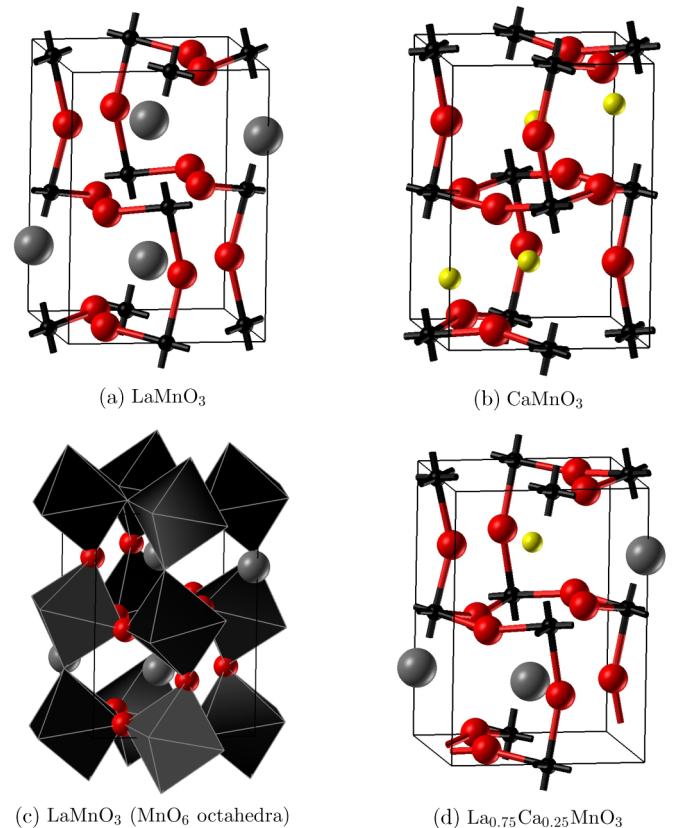(c) LaMnO$_3$ (MnO$_6$ octahedra)   (d) La$_{0.75}$Ca$_{0.25}$MnO$_3$

FIG. 1. (Color online) Crystallographic cells at the geometries indicated in Tables I and III for the ground state parent and doped compounds, where **b** is the longest lattice vector. Large (gray), medium (red), and small (black) spheres correspond to the La, O, and Mn atoms, respectively, in (a); the additional atom (yellow) in (b) and (c) is the Ca atom.

above, is expected to be more reliable than LDA or GGA approaches [51,52]. The exchange and correlation potentials and energy functional are integrated numerically on an atom centered grid of points. The integration over radial and angular coordinates is performed using Gauss-Legendre and Lebedev schemes, respectively. A pruned grid consisting of 99 radial points and five subintervals with (146, 302, 590, 1454, 590) angular points has been used for all calculations (the XXLGRID option implemented in CRYSTAL09 [63]). This grid converges the integrated charge density to an accuracy of about $\times 10^{-6}$ electrons per unit cell. The Coulomb and exchange series are summed directly and truncated using overlap criteria with thresholds of 10^{-7}, 10^{-7}, 10^{-7}, 10^{-7}, and 10^{-14} as described previously [63,64]. Reciprocal space sampling was performed on a Pack-Monkhorst net with a shrinking factor IS = 8, which defines 75 symmetry unique k points in the bulk structure for the endpoint compounds. The self-consistent field procedure was converged up to a tolerance in the total energy of $\Delta E = 1 \times 10^{-7} E_h$ per unit cell. Population analysis of the charge and spin densities and the projection of the density of states (DOS) is performed using a Mulliken partitioning.

The cell parameters and the internal coordinates have been determined by minimization of the total energy within an iterative procedure based on the total energy gradient calculated analytically with respect to the cell parameters and nuclear coordinates. Convergence was determined from the root mean square (rms) and the absolute value of the largest component of the forces. The thresholds for the maximum and the rms forces (the maximum and the rms atomic displacements) have been set to 0.000 45 and 0.000 30 (0.001 80 and 0.0012) in

atomic units. Geometry optimization was terminated when all four conditions were satisfied simultaneously.

III. RESULTS

A. Structural, magnetic, and electronic properties of the endpoint compounds: LaMnO$_3$ and CaMnO$_3$

The *Pnma* orthorhombic crystallographic cells for the endpoint compounds are shown in Figs. 1(a) and 1(b). The optimized and experimental lattice parameters of the ground state and metastable magnetic structures are reported in Table I. The percentage difference between the optimized structure for the ground state and the corresponding low-temperature experimental one is also given.

For LaMnO$_3$, the calculated lattice parameters **b** and **c** are in good agreement with the experimental values; the percentage errors are 0.82% and 1.41%, respectively. The **a** lattice parameter is overestimated by 4.89%. There is no experimental certainty for this parameter, since values between 5.472 and 5.748 Å are reported [65]. Moreover, LaMnO$_3$ shows oxidative nonstoichiometry, which structurally implies excess oxygen, or cation vacancies [66,67]. The lattice vectors are sensitive to the stoichiometry of the sample and decrease with increasing oxygen content [68,69]. The variation of the lattice parameters with temperature is not significant, since the estimated thermal expansion is 0.08% between 9 K and room temperature (RT).

The optimized cell parameters determined from other theoretical methods are also shown in Table I. In one case,

TABLE I. Optimized and experimental lattice parameters for the endpoint compounds for various magnetic structures. In the fourth column, the arrows refer to the spin arrangement of the four Mn atoms shown in Fig. 1. The percentage difference between the ground state magnetic structure and the corresponding low-temperature experimental one [AFM (*A*) for LaMnO$_3$ and AFM (*G*) for CaMnO$_3$] is given in italics. The energy difference with respect to the ground state for each compound ΔE is also reported in meV per formula unit.

Compound	Method	Magnetic type	Spin ordering	**a** (Å)	**b** (Å)	**c** (Å)	V (Å^3)	ΔE (meV)	T (K)	Ref.
			Optimized cell							
LaMnO$_3$	B3LYP	AFM (*C*)	↑↓↓↑	6.055	7.739	5.598	262.3	27.3		
	B3LYP	AFM (*G*)	↑↓↑↓	6.076	7.713	5.600	262.4	22.7		
	B3LYP	FM (*F*)	↑↑↑↑	5.995	7.758	5.613	261.1	5.1		
	B3LYP	AFM (*A*)	↑↑↓↓	6.010	7.735	5.614	261.0	0.0		
				4.89%	*0.82%*	*1.41%*	*6.74%*			
	UHF	AFM (*A*)	↑↑↓↓	5.740	7.754	5.620	249.3			[44]
	GGA	AFM (*A*)	↑↑↓↓	5.753	7.721	5.559	246.9			[41]
			Experimental cell							
		AFM (*A*)	↑↑↓↓	5.699	7.718	5.539	243.6		RT	[70]
		AFM (*A*)	↑↑↓↓	5.505	7.807	5.544	238.3		190	[71]
		AFM (*A*)	↑↑↓↓	5.730	7.672	5.536	243.4		9	[69]
			Optimized cell							
CaMnO$_3$	B3LYP	FM (*F*)	↑↑↑↑	5.319	7.515	5.328	213.0	31.3		
	B3LYP	AFM (*A*)	↑↓↓↑	5.298	7.519	5.328	212.2	11.7		
	B3LYP	AFM (*C*)	↑↑↓↓	5.318	7.495	5.332	212.5	3.5		
	B3LYP	AFM (*G*)	↑↓↑↓	5.302	7.505	5.330	212.1	0.0		
				0.49%	*0.87%*	*1.41%*	*2.73%*			
			Experimental cell							
		AFM (*G*)	↑↓↑↓	5.279	7.448	5.264	207.0		RT	[72]
		AFM (*G*)	↑↓↑↓	5.276	7.440	5.256	206.3		10	[73]

TABLE II. Optimized and experimental Mn-O bond lengths for the endpoint compounds, where N is the number of neighbors. The experimental bond lengths have been calculated based on unit cell dimensions and atomic coordinates determined from neutron powder-diffraction studies at 9 K [69,72]. The lattice vectors corresponding to the low-temperature structures considered here are given in Table I.

Compound	N	Optimized Mn-O (Å)	Experimental Mn-O (Å)	% difference
$LaMnO_3$	2	1.919	1.91	0.47
	2	1.986	1.96	1.32
	2	2.310	2.18	5.96
$CaMnO_3$	2	1.916	1.90	0.84
	2	1.917	1.90	0.89
	2	1.919	1.90	0.99

the UHF level of theory is used [44], while the GGA to DFT is adopted in the other [41]. Although both predict a value of **a** close to the upper limit observed experimentally, the GGA and UHF calculations obtain a FM ground state and fail to predict the experimental ground state with A-type antiferromagnetic (A-AFM) ordering [41,42].

The ionic radius mismatch between La^{3+} (1.03 Å) and Ca^{2+} (1.00 Å) [74] leads to a contraction in all lattice dimensions (**a**, **b**, and **c**) for $CaMnO_3$. The calculated lattice parameters are in good agreement with the cited low-temperature (10 K) $Pnma$ experimental phase determined by neutron powder diffraction and the percentage errors are all within 1% of the experimental values. In Table I, it can be seen that the estimated thermal expansion for $CaMnO_3$ is 0.34% for the temperature range 10 K to RT.

$LaMnO_3$ and $CaMnO_3$ have essentially the same structure: Each Mn ion is sixfold coordinated with O ions, which form an octahedral cage around the Mn ion, shown in Fig. 1(c). A first approximation to the electronic structure of both compounds is provided by the ionic model. The Mn ions have a formal charge of 3+ and a $3d^4$ configuration. In the MnO_6 octahedron the Mn d orbitals are split into triply degenerate t_{2g} and doubly degenerate e_g manifolds. The e_g degeneracy is lifted by a Jahn-Teller (JT) distortion of the MnO_6 octahedra, as is evident from the Mn-O bond lengths of $LaMnO_3$, reported in Table II. There are two long (apical) and two pairs of shorter (equatorial) Mn-O bond lengths, due to the presence of JT distorted 3+ sites. The two longer equatorial bond lengths are directed along the **b** lattice vector. The optimized B3LYP bond lengths are comparable to the experimental bond lengths, determined from diffraction studies [75]. For $LaMnO_3$, the apical bond lengths are overestimated by 6%. Note that these bonds are in the plane defined by **a** and **c** and have a large component along **a**. Hence, this discrepancy is related to the overestimated **a** lattice vector, for which there is considerable uncertainty in the measurement.

In $CaMnO_3$, the Mn ions have a formal charge of 4+ with a $3d^3$ configuration. The Mn-O bond lengths for this composition are uniform when compared to those of $LaMnO_3$, since the octahedra are not JT distorted. There is a good agreement with the experimental bond lengths obtained from diffraction studies [69], which are shown in Table II. The percentage errors are all within 1% of the experimental values. Therefore, the longer **a** lattice vector in $LaMnO_3$ is primarily attributed to the cooperative JT distortion, which is not present in $CaMnO_3$.

The low-temperature orthorhombic phase of $LaMnO_3$ has an A-type ordering of the spins (see Fig. 2), which consists of ferromagnetic MnO_2 planes coupled antiferromagnetically along the **b** axis. Here, the F-, C-, and G-type spin configurations are also considered (shown in Fig. 2) and the energy difference per formula unit (f.u.) ΔE (meV) at fixed geometry with respect to the ground state is reported in Table I. The ground state of $CaMnO_3$ is found to be a G-type antiferromagnet, where the nearest-neighbor spin moments are coupled antiferromagnetically along the **b** axis and in the **ac** plane. As seen in Table I, the spin configurations adopted do not have a significant effect on the lattice parameters of $LaMnO_3$ or $CaMnO_3$.

Figures 3(a) and 3(b) show the total electronic density of states (DOS) for $LaMnO_3$ and $CaMnO_3$, respectively, with projections onto the La, Ca, Mn, and O atoms. $LaMnO_3$ is predicted to be an insulator with a fundamental direct band gap of 3.22 eV, which is larger than the reported experimental value of 1.1 eV [76,77] from optical measurements. The indirect band gap of 2.66 eV that can be seen in B3LYP typically overestimates band gaps in ionic systems due to inadequacy of the theory and also to the neglect of excitonic binding. This discrepancy is, however, somewhat larger than expected and
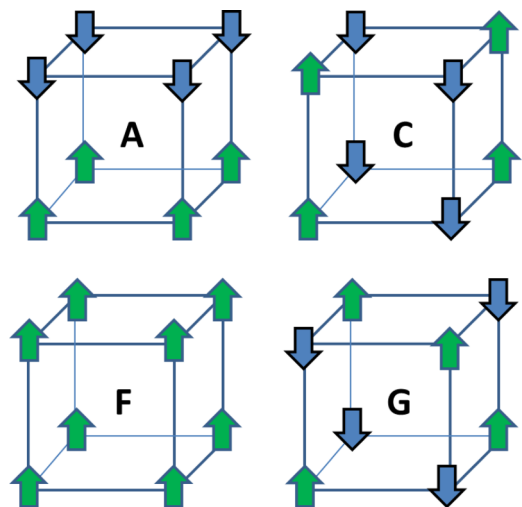

FIG. 2. (Color online) The A-, C-, F-, and G-type collinear spin configurations considered, where the arrows indicate the ordering of Mn spin moments.

(a) AFM (A-type) LaMnO$_3$

(b) AFM (G-type) CaMnO$_3$

(c) FM La$_{0.75}$Ca$_{0.25}$MnO$_3$ delocalized

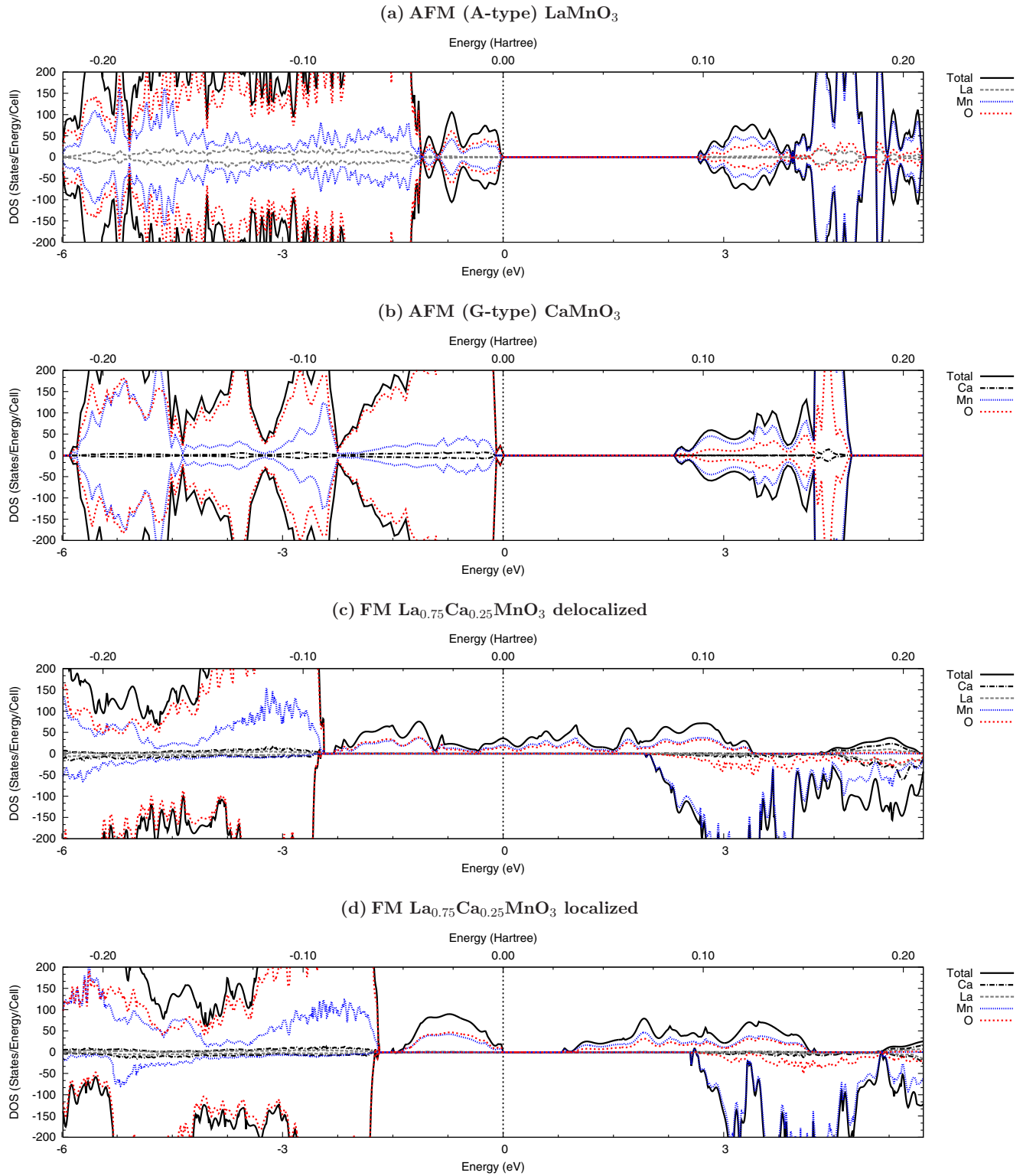**(d) FM La$_{0.75}$Ca$_{0.25}$MnO$_3$ localized**

FIG. 3. (Color online) Total density of states with projections on the Ca, La, Mn, and O atoms; the Fermi level is at 0 eV.

may be due to the effects of defects [66–68] on the optical spectrum. The lower valence band DOS is mainly attributed to the O $2p$ and Mn $3d$ bands, which hybridize, indicating partial covalency. The O $2p$ and Mn $3d$ bands also dominate the conduction band. The calculated band gap for CaMnO$_3$ of

2.35 eV is comparable with the value of 3.1 eV [77] deduced from frequency dependent optical-conductivity spectra. The lower valence band DOS isattributed to the O $2p$ bands and the conduction band is dominated by O $2p$ and Mn $3d$ bands. The JT-split Mn$(3d)e_g^1$ is depleted at $x = 1$ and, therefore,
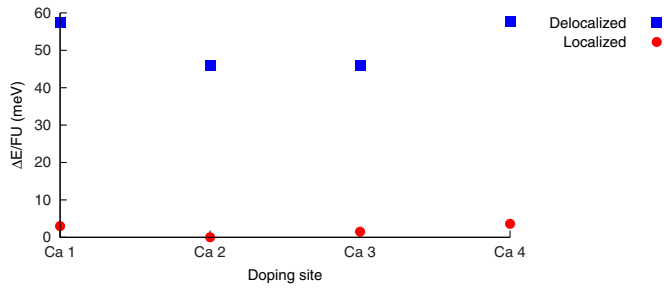
FIG. 4. (Color online) Energy difference (ΔE) per formula unit (f.u.) with respect to the ground state [FM with hole localized at Ca site (2)] as a function of doping site for both the localized and delocalized hole solutions in the optimized ground state geometry. In the case of the delocalized hole solution, site (1) is equivalent to (4), and (2) to (3) by symmetry.
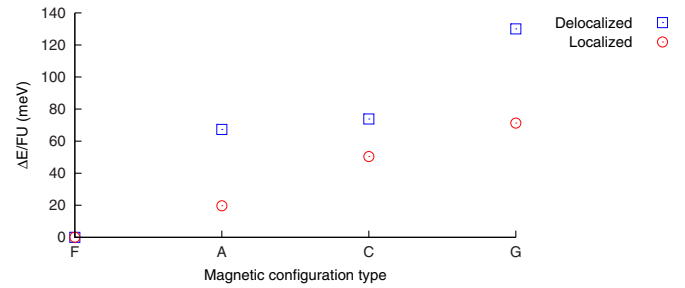

FIG. 5. (Color online) Energy difference (ΔE) per formula unit (f.u.), with respect to the localized and delocalized hole solutions at the optimized ground state geometry, as a function of the spin configurations (types F, A, C, G).

CaMnO$_3$ is also an insulator. Both the A-type AFM LaMnO$_3$ and G-type AFM CaMnO$_3$ ground state phases are used as reference electronic structures for interpreting the effects of doping, which are discussed below.

B. La$_{0.75}$Ca$_{0.25}$MnO$_3$ (ordered Ca distribution)

The distribution of Ca in La$_{1-x}$Ca$_x$MnO$_3$ at $x = 0.25$ is substitutionally disordered, since neutron diffraction data have been fitted with structure factors based on a partial occupation of Ca sites [16]. The disordered structure of La$_{0.75}$Ca$_{0.25}$MnO$_3$ has been approximated by an ordered Ca distribution [see Fig. 1(b)], where a La atom has been replaced by a Ca atom in the unit cell of LaMnO$_3$. Within an ionic model, the hole concentration for La$_{0.75}$Ca$_{0.25}$MnO$_3$ is 1/4. The doped hole (one per unit cell) could delocalize in the O $2p$ band or localize on an O site. Alternatively, a solution in which the hole delocalizes in the Mn bands, or localizes on a particular Mn, is also possible. Based on the DOS, the upper valence band is a mixture of O and Mn states. The ground state is not clear *a priori*, even in a rigid band model.

In general, by varying the initial density matrix, it is possible to converge various solutions in strongly correlated systems. Here, the calculations with a delocalized hole in the O $2p$ band do not converge to a stable solution. Hence, the electronic structures and energetics of the following two stable solutions that were found are compared: (1) the localization of the hole on a particular Mn ion with a consequent change in the oxidation state (from Mn^{3+} to Mn^{4+}) and (2) the delocalization of the hole over two Mn ions.

A local distortion of the lattice is expected due to the difference in ionic radii between La^{3+} (1.032 Å) and Ca^{2+} (1.000 Å) [74], as well as the difference between Mn^{3+} (0.645 Å) and Mn^{4+} (0.530 Å) [74]. The latter is larger and is attributed to the localization of the hole on a particular Mn and the consequent formation of an anti-JT polaron, in which the degenerate e_g orbital is not occupied. This is direct evidence of a very strong charge-lattice interaction. Consequently, the symmetry between the La sites is removed and there is a dependence of the energetics on the dopant site, in addition to the localization versus delocalization of the hole (shown in Fig. 4). In the predicted ground state, a hole localizes on a particular Mn. If one considers a conductivity model, where a localized hole is thermally activated to a conducting state over an energy barrier (also referred to as the hopping barrier herein), then a $\Delta E_{\text{hopping}}$ of 46 meV (per formula unit) is required to delocalize the hole with respect to the localized ground state. This is much larger than the energy variation with the site of the dopant (order of 6–12 meV), as can be seen in Fig. 4. The Ca-Mn bond distances are longer for the energetically more favorable states [Ca sites (2) and (3)] when compared to the metastable states [Ca sites (1) and (4)]. This is consistent with a simple electrostatic picture in which the Ca ion and hole repel each other. The change in energy ΔE for spin configuration types F, A, C, and G [for the most stable doping site, Ca site (2)] is also shown in Fig. 5. The ferromagnetic spin configuration is found to be the ground state for both the localized and delocalized hole solutions.

TABLE III. Optimized and experimental [16] lattice parameters for the orthorhombic (O) and monoclinic (M) structures of the doped compound. The percentage difference between the calculated ground state structure and the corresponding experimental one is given in italics. D and L correspond to the delocalized and localized hole solutions, respectively.

	ΔE (meV)	Structure	**a** (Å)	**b** (Å)	**c** (Å)	α (deg)	β (deg)	γ (deg)	V (Å^3)
D	65.8	O	5.652	7.791	5.556	90.0	90.0	90.0	244.7
D	45.8	M	5.635	7.812	5.569	90.0	87.8	90.0	244.8
L	5.56	O	5.631	7.843	5.548	90.0	90.0	90.0	245.0
L	0.00	M	5.622	7.842	5.559	90.3	89.4	90.0	245.1
Expt.		O	5.470	7.734	5.489	90.0	90.0	90.0	232.2
			2.70%	*1.38%*	*1.26%*				

TABLE IV. Optimized Mn-O bond lengths for the $La_{0.75}Ca_{0.25}MnO_3$ unit cell in the FM-I and FM-M states.

Mn atom	Mn-O bond length (Å) metal	Mn-O bond length (Å) insulator
1	1.933	1.885
	1.954	1.903
	1.954	2.043
	2.018	2.114
	2.172	2.125
	2.209	2.146
2	1.914	1.907
	1.929	1.919
	1.967	2.042
	2.006	2.091
	2.026	2.103
	2.027	2.122
3	1.914	1.914
	1.929	1.928
	1.967	1.939
	2.006	1.940
	2.026	1.962
	2.027	1.973
4	1.933	1.880
	1.954	1.938
	1.954	2.047
	2.018	2.071
	2.172	2.114
	2.209	2.141

The lattice parameters for the ground state (FM with a localized hole), metastable state (delocalized hole), and the experimental geometry are given in Table III. It is evident that there is deviation from the orthorhombic symmetry, particularly the β angle value (see Table III). This is attributed to the ordered distribution of Ca implied in the simulation,

which leads to a cooperative distortion in a periodic structure when compared to the disordered distribution in the observed material. The delocalized and localized hole solutions for the *Pnma* orthorhombic structure are considered (α, β, and γ are 90°), and are also shown in Table III. The energy difference between the monoclinic and orthorhombic localized hole solutions is of the order of 6 meV. This is an approximation to the energy scale required to alter the Ca distribution, which suggests that at RT a disordered distribution is expected, as observed experimentally [16].

A distortion of the geometry occurs when the hole localizes. This is evident from the Mn-O nearest-neighbor bond lengths in Table IV. In the insulating state, it can be seen that the JT distortion of the MnO_6 octahedron associated with Mn(3) is lifted, since the bond lengths are more homogeneous when compared to those of the Mn(1), Mn(2), and Mn(4) centered octahedra in the unit cell. This is attributed to the localized hole, which induces an antipolaronic distortion. In particular, this observation is in agreement with neutron diffraction experiments, where the local JT distortion in the insulating phase for $LaMnO_3$ decreases continuously with increasing Ca content [78]. To understand the distortions mentioned above, the spin moment of the Mn atoms is indicated in Table V. In the localized case there are four inequivalent Mn atoms, the number of possible spin configurations is larger than the delocalized case where two Mn atoms are inequivalent. The average magnetic moment for the delocalized case is $3.7 \mu_B$/Mn. This is in good agreement with the experimental ferromagnetic moment of $3.4 \mu_B$/Mn [79].

The magnetic phases for $LaMnO_3$ and $La_{0.75}Ca_{0.25}MnO_3$ with corresponding spin density plots are shown in Fig. 6. It can be seen that the magnetic coupling switches from antiferromagnetic ($LaMnO_3$) to ferromagnetic ($La_{0.75}Ca_{0.25}MnO_3$). Polarization of the O $2p$ orbitals by the Mn $3d$ is evident, and this is expected to affect the superexchange coupling mechanism. The computed magnetic coupling constant J between Mn ions can be analyzed in terms of a simple superexchange model. J, which is positive for FM and

TABLE V. Relative energies of various spin configurations per formula unit (f.u.) with respect to the ground state in the delocalized and localized hole optimized geometries. The total spin and Mn spin moments are also shown.

| Geometry	Spin configuration	ΔE/f.u. (meV)	Total spin	Mn(1) (μ_B)	Mn(2) (μ_B)	Mn(3) (μ_B)	Mn(4) (μ_B)
Delocalized	↑↑↑↑	0.0	15.0	3.86	3.52	3.52	3.86
	↓↑↑↑	45.0	7.00	−3.73	3.36	3.55	3.82
	↑↓↓↑	67.3	1.00	3.77	−3.40	−3.40	3.77
	↑↑↓↓	73.8	0.00	3.87	3.41	−3.45	−3.88
	↑↓↑↑	102.5	7.00	3.73	−3.63	3.12	3.82
	↑↓↑↓	130.4	−1.00	3.73	−3.68	2.81	−3.75
Localized	↑↑↑↑	0.0	15.0	3.82	3.81	3.15	3.80
	↑↑↓↓	19.7	1.00	3.83	3.82	−3.05	−3.71
	↑↑↑↓	34.3	7.00	3.82	3.81	2.94	−3.73
	↑↓↓↓	34.8	−7.00	3.74	−3.73	−3.14	−3.71
	↑↑↓↑	35.0	9.00	3.82	3.81	−2.82	3.82
	↑↓↑↑	36.2	7.00	3.73	−3.74	3.05	3.80
	↑↓↓↑	50.4	1.00	3.73	−3.73	−2.94	3.82
	↑↓↑↓	71.3	−1.00	3.74	−3.74	2.83	−3.73

(a) LaMnO$_3$ A-AFM (b) La$_{0.75}$Ca$_{0.25}$MnO$_3$ FM
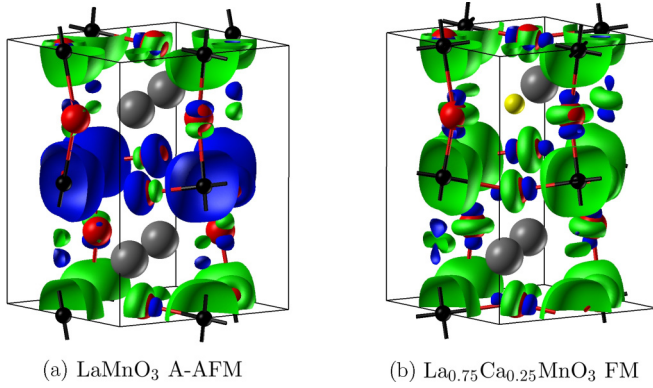
FIG. 6. (Color online) Isovalue surfaces of the calculated spin density for (a) LaMnO$_3$ and (b) La$_{0.75}$Ca$_{0.25}$MnO$_3$. The spin isosurface values are as follows: Green is 0.005 (spin up) and blue is -0.005 (spin down); in units of $|e|/$bohr^3.

negative for AFM interactions, has been obtained from $\Delta E = E^{\mathrm{AFM}} - E^{\mathrm{FM}}$, the difference of total energies of ferromagnetic and antiferromagnetic phases. ΔE is proportional to J and is given by $\Delta E = NZJS_z S_z'$, where N is the number of symmetric Mn atoms in the ferromagnetic cell, Z is the number of the next-nearest (Mn) neighbors to each of the N Mn with opposite spin, and $S_z S_z'$ is the product of the z component of neighboring Mn spin moments, according to the Ising Hamiltonian. The calculation of J is carried out by assuming the following: (1) For the localized hole solution, the octahedron is affected by a large distortion and all Mn-O distances are different. The quantities J_{eq} and J_{ap} are an average and do not take into account the differences in Mn-O bond length. (2) The value of S_z is $3.75\mu_B$/Mn, which assumes the solution of one delocalized hole over all four Mn atoms. Under these assumptions a mapping of the DFT energetics to the superexchange model can be achieved and J_{ap} and J_{eq} determined (see Appendix). The computed coupling constants are given in Table VI. It is evident that J_{ap} and J_{eq} for the localized hole solution (FM-I) are smaller than those for the delocalized hole (FM-M).

Figures 3(c) and 3(d) show the projected density of states (PDOS) for a La$_{0.75}$Ca$_{0.25}$MnO$_3$ metal and a La$_{0.75}$Ca$_{0.25}$MnO$_3$ insulator, respectively (the total and projected density of states of LaMnO$_3$ and CaMnO$_3$ are also shown for comparison purposes). Zero energy corresponds to the Fermi level, so occupied and unoccupied states are characterized by negative and positive energies, respectively. Through chemical substitution of a Ca atom into the local La site, a transition to a FM half-metallic state occurs as can be seen in Fig. 3(c). This is in agreement with the half metallicity reported experimentally

TABLE VI. Calculated J_{eq} and J_{ap} in meV for the delocalized and localized hole solutions.

	J_{ap} (meV)	J_{eq} (meV)
Delocalized	10.5	4.78
Localized	2.62	3.36

from scanning tunneling spectroscopy measurements [80]. This provides direct evidence for the fact that B3LYP describes the electronic properties of the observed material correctly. The spin resolved band gap of 2.02 eV in the majority and 4.22 eV in the minority spin states is evident in Fig. 3(d), and this is attributed to the formation of an anti-JT polaron. In Figs. 3(b) and 3(c), the hybridization of the Mn d and O p majority spin states just below E_f is clearly evident. Both Mn and O contribute to the DOS at E_f.

IV. CONCLUSIONS

Hybrid-exchange DFT calculations have been used to correctly predict the very different structural and magnetic symmetries of the endpoint compounds, LaMnO$_3$ and CaMnO$_3$. The most stable phase predicted for an ordered Ca distribution in La$_{0.75}$Ca$_{0.25}$MnO$_3$ is the ferromagnetic-insulating state. An anti-Jahn-Teller polaron forms and the localized state is influenced by long range cooperative Jahn-Teller distortions. We have deduced that the relative energy scales are of a similar magnitude, which indicates strong coupling between charge, orbital, spin, and lattice degrees of freedom. The present study demonstrates the reliability of the description of the hybrid B3LYP functional for strongly correlated systems, such as the La$_{1-x}$A$_x$MnO$_3$ manganite series. This work provides a basis for further much more computationally demanding investigations, aimed at determining the effect of a disordered Ca distribution on the structural, magnetic, and electronic properties of La$_{1-x}$Ca$_x$MnO$_3$.

APPENDIX

The exchange coupling constants J_{eq} and J_{ap} for the delocalized hole case are determined from the following:

$$\Delta E = E^{\mathrm{AFM}}_{\uparrow\uparrow\downarrow\downarrow} - E^{\mathrm{FM}} = NZJ_{\mathrm{ap}}\hat{S}_z^2 = 4 \times 2 \times J_{\mathrm{ap}}\left(3.75 * \tfrac{1}{2}\right)^2, \tag{A1}$$

$$\Delta E = E^{\mathrm{AFM}}_{\uparrow\downarrow\downarrow\uparrow} - E^{\mathrm{FM}} = NZJ_{\mathrm{eq}}\hat{S}_z^2 = 4 \times 4 \times J_{\mathrm{eq}}\left(3.75 * \tfrac{1}{2}\right)^2. \tag{A2}$$

In addition, J_{ap} and J_{eq} for the localized hole solution can be calculated from the following:

$$\Delta E = E^{AFM}_{\uparrow\uparrow\downarrow\downarrow} - E^{FM} = NZJ_{ap}\hat{S}_z^2 = 2 \times 2 \times J_{ap}\left[\left(4*\tfrac{1}{2} \times 4*\tfrac{1}{2}\right) + \left(3*\tfrac{1}{2} \times 4*\tfrac{1}{2}\right)\right], \tag{A3}$$

$$\Delta E = E^{AFM}_{\uparrow\downarrow\downarrow\uparrow} - E^{FM} = NZJ_{eq}\hat{S}_z^2 = 2 \times 4 \times J_{eq}\left[\left(4*\tfrac{1}{2} \times 4*\tfrac{1}{2}\right) + \left(4*\tfrac{1}{2} \times 3*\tfrac{1}{2}\right)\right]. \tag{A4}$$

[1] G. H. Jonker and J. H. Santen, Physica **16**, 337 (1950).

[2] J. G. Bednerz and K. A. Müller, Z. Phys. B **64**, 189 (1986).

[3] M. K. Wu, J. R. Ashburn, C. J. Torng, P. H. Hor, R. L. Meng, L. Gao, Z. J. Huang, Y. Q. Wang, and C. W. Chu, Phys. Rev. Lett. **58**, 908 (1987).

[4] R. von Helmolt, J. Wecker, B. Holzapfel, L. Schultz, and K. Samwer, Phys. Rev. Lett. **71**, 2331 (1993).

[5] S. Jin, T. H. Tiefel, M. McCormack, R. A. Fastnacht, R. Ramesh, and L. H. Chen, Science **264**, 413 (1994).

[6] M. B. Salamon and M. Jaime, Rev. Mod. Phys. **73**, 583 (2001).

[7] K. A. Gschneidner, V. K. Pecharsky, and A. O. Tsokol, Rep. Prog. Phys. **68**, 1479 (2005).

[8] K. A. Gschneidner and V. K. Pecharsky, Annu. Rev. Mater. Sci. **30**, 387 (2000).

[9] M. Phan and S. Yu, J. Magn. Magn. Mater. **308**, 325 (2007).

[10] C. N. R. Rao and B. Raveau, *Colossal Magnetoresistance, Charge Ordering and Related Properties of Manganese Oxides* (World Scientific, Singapore, 1998).

[11] E. Dagotto, T. Hotta, and A. Moreo, Phys. Rep. **344**, 1 (2001).

[12] Y. Tokura, *Colossal Magnetoresistance Oxides* (Gordon and Breach, London, 1999).

[13] A. J. Morelli, A. M. Mance, J. V. Mantese, and A. L. Micheli, J. Appl. Phys. **79**, 373 (1996).

[14] P. Schiffer, A. P. Ramirez, W. Bao, and S.-W. Cheong, Phys. Rev. Lett. **75**, 3336 (1995).

[15] M. H. Phan, S. C. Yu, Y. M. Moon, and N. H. Hur, J. Magn. Magn. Mater. **272–276**, e503 (2004).

[16] P. G. Radaelli, G. Iannone, M. Marezio, H. Y. Hwang, S.-W. Cheong, J. D. Jorgensen, and D. N. Argyriou, Phys. Rev. B **56**, 8265 (1997).

[17] Q. T. Phung, V. K. Vu, A. B. Ngac, H. S. Nguyen, and N. N. Hoang, J. Magn. Magn. Mater. **324**, 2363 (2012).

[18] R. K. Zheng, A. N. Tang, Y. Yang, W. Wang, G. Li, and X. G. Li, J. Appl. Phys. **94**, 514 (2003).

[19] J. Alonso, E. Herrero, J. M. González-Calbet, M. Vallet-Regí, J. L. Martinez, J. M. Rojo, and A. Hernando, Phys. Rev. B **62**, 11328 (2000).

[20] J. Mira, J. Rivas, L. E. Hueso, F. Rivadulla, M. A. Lopes Quintela, M. A. Senarís Rodríguez, and C. A. Ramos, Phys. Rev. B **65**, 024418 (2001).

[21] T. L. Aselage, D. Emin, S. S. McCready, E. L. Venturini, M. A. Rodriguez, J. A. Voigt, and T. J. Headley, Phys. Rev. B **68**, 134448 (2003).

[22] X. X. Zhang, J. Tejada, Y. Xin, G. F. Sun, K. W. Wong, and X. Bohigas, Appl. Phys. Lett. **69**, 3596 (1996).

[23] J. L. Cohn, J. J. Neumeier, C. P. Popoviciu, K. J. McClellan, and T. Leventouri, Phys. Rev. B **56**, R8495 (1997).

[24] Z. B. Guo, Y. W. Du, J. S. Zhu, H. Huang, W. P. Ding, and D. Feng, Phys. Rev. Lett. **78**, 1142 (1997).

[25] Y. Sun, X. Xu, and Y. Zhang, J. Magn. Magn. Mater. **219**, 183 (2000).

[26] C. Zener, Phys. Rev. **82**, 403 (1951).

[27] C. Zener, Phys. Rev. **81**, 440 (1951).

[28] A. J. Millis, P. B. Littlewood, and B. I. Shraiman, Phys. Rev. Lett. **74**, 5144 (1995).

[29] A. J. Millis, R. Mueller, and B. I. Shraiman, Phys. Rev. B **54**, 5405 (1996).

[30] J. M. de Teresa, M. R. Ibarra, P. A. Algarabel, C. Ritter, C. Marquina, J. Blasco, A. del Moral, and Z. Arnold, Nature (London) **386**, 256 (1997).

[31] T. A. Tyson, J. Mustre de Leon, S. D. Conradson, A. R. Bishop, J. J. Neumeier, H. Roder, and J. Zang, Phys. Rev. B **53**, 13985 (1996).

[32] S. J. L. Billinge, R. G. DiFrancesco, G. H. Kwei, J. J. Neumeier, and J. D. Thompson, Phys. Rev. Lett. **77**, 715 (1996).

[33] C. H. Booth, F. Bridges, G. H. Kwei, J. M. Lawrence, A. L. Cornelius, and J. J. Neumeier, Phys. Rev. Lett. **80**, 853 (1998).

[34] A. Lanzara, N. L. Saini, M. Brunelli, F. Natali, A. Bianconi, P. G. Radaelli, and W. Cheong, Phys. Rev. Lett. **81**, 878 (1998).

[35] N. P. Konstantinidis and C. H. Patterson, Phys. Rev. B **70**, 064407 (2004).

[36] C. H. Patterson, Phys. Rev. B **72**, 085125 (2005).

[37] E. A. Ahmad, L. Liborio, D. Kramer, G. Mallia, A. R. Kucernak, and N. M. Harrison, Phys. Rev. B **84**, 085137 (2011).

[38] H. Chevreau, I. de P. R. Moreira, B. Silvi, and F. Illas, J. Phys. Chem. **105**, 3570 (2001).

[39] W. E. Pickett and D. J. Singh, Phys. Rev. B **53**, 1146 (1996).

[40] H. Sawada, Y. Morikawa, K. Terakura, and N. Hamada, Phys. Rev. B **56**, 12154 (1997).

[41] E. A. Kotomin, R. A. Evarestov, and Y. A. Mastrikov, Phys. Chem. Chem. Phys. **7**, 2346 (2005).

[42] T. Hashimoto, S. Ishibashi, and K. Terakura, Phys. Rev. B **82**, 045124 (2010).

[43] Y.-S. Su, T. A. Kaplan, S. D. Mahanti, and J. F. Harrison, Phys. Rev. B **61**, 1324 (2000).

[44] M. Nicastro and C. H. Patterson, Phys. Rev. B **65**, 205111 (2002).

[45] D. Munoz, N. M. Harrison, and F. Illas, Phys. Rev. B **69**, 085115 (2004).

[46] S. Satpathy, Z. S. Popović, and F. R. Vukajlović, J. Appl. Phys. **79**, 4555 (1996).

[47] G. Trimarchi and N. Binggeli, Phys. Rev. B **71**, 035101 (2005).

[48] V. I. Anisimov, J. Zaanen, and O. K. Andersen, Phys. Rev. B **44**, 943 (1991).

[49] V. I. Anisimov, I. V. Solovyev, M. A. Korotin, M. T. Czyzyk, and G. A. Sawatzky, Phys. Rev. B **48**, 16929 (1993).

[50] T. Geng, Phys. Lett. A **372**, 533 (2007).

[51] J. Muscat, A. Wander, and N. M. Harrison, Chem. Phys. Lett. **342**, 397 (2001).

[52] F. Cora, M. Alfredsson, G. Mallia, D. S. Middlemiss, W. C. Mackrodt, R. Dovesi, and R. Orlando, *The Performance of Hybrid Density Functionals in Solid State Chemistry* (Springer, Berlin, 2004), Vol. 113.

[53] G. Mallia and N. M. Harrison, Phys. Rev. B **75**, 165201 (2007).

[54] N. C. Wilson, S. P. Russo, J. Muscat, and N. M. Harrison, Phys. Rev. B **72**, 024110 (2005).

[55] G. C. De Fusco, B. Montanari, and N. M. Harrison, Phys. Rev. B **82**, 220404 (2010).

[56] L. Ge, J. H. Jefferson, B. Montanari, N. M. Harrison, G. G. Petifor, and G. A. D. Briggs, ACS Nano **3**, 1069 (2009).

[57] G. C. De Fusco, L. Pisani, B. Montanari, and N. M. Harrison, Phys. Rev. B **79**, 085201 (2009).

[58] L. Liborio, G. Mallia, and N. M. Harrison, Phys. Rev. B **79**, 245133 (2009).

[59] C. L. Bailey, L. Liborio, G. Mallia, S. Tomić, and N. M. Harrison, J. Phys.: Conf. Ser. **242**, 012004 (2010).

[60] L. Liborio, C. L. Bailey, G. Mallia, S. Tomić, and N. M. Harrison, J. Appl. Phys. **109**, 023519 (2011).

[61] J. M. Ricart, R. Dovesi, C. Roetti, and V. R. Saunders, Phys. Rev. B **52**, 2381 (1995).

[62] I. P. R. Moreira and F. Illas, Phys. Rev. B **55**, 4129 (1997).

[63] R. Dovesi, V. R. Saunders, C. Roetti, R. Orlando, C. M. Zicovich-Wilson, F. Pascale, B. Civalleri, K. Doll, N. M. Harrison, I. J. Bush *et al.*, *CRYSTAL09 User's Manual* (University of Torino, Torino, 2009).

[64] C. Pisani, R. Dovesi, and C. Roetti, *Hartree-Fock ab initio Treatment of Crystalline Systems*, Lecture Notes in Chemistry Vol. 48 (Springer, Heidelberg, 1988).

[65] http://cds.dl.ac.uk/icsd

[66] J. A. M. van Roosmalen, E. H. P. Cordfunke, R. B. Helmholdt, and H. W. Zandbergen, J. Solid State Chem. **110**, 100 (1994).

[67] B. C. Tofield and W. R. Scott, J. Solid State Chem. **10**, 183 (1974).

[68] J. A. M. van Roosmalen, P. van Vlaanderen, E. H. P. Cordfunke, W. L. IJdo, and D. J. W. IJdo, J. Solid State Chem. **114**, 516 (1995).

[69] B. C. Hauback, H. Fjellvg, and N. Sakai, J. Solid State Chem. **124**, 43 (1996).

[70] P. Norby, I. G. K. Andersen, and E. K. Andersen, J. Solid State Chem. **119**, 191 (1995).

[71] V. Dyakonov, F. N. Bukhanko, V. I. Kamenev, E. E. Zubov, M. Arciszewska, W. Dobrowolski, V. Mikhaylov, R. Puźniak, A. Wiśniewski, K. Piotrowski *et al.*, Phys. Rev. B **77**, 214428 (2008).

[72] K. R. Poeppelmeier, M. E. Leonowicz, J. C. Scanlon, and J. M. Longo, J. Solid State Chem. **45**, 71 (1982).

[73] E. Božin, A. Sartbaeva, H. Zheng, S. Wells, J. Mitchell, T. Proffen, M. F. Thorpe, and S. J. L. Billinge, J. Phys. Chem. Solids **69**, 2146 (2008).

[74] R. D. Shannon, Acta Crystallogr., Sect. A **32**, 751 (1976).

[75] C. H. Booth, F. Bridges, G. H. Kwei, J. M. Lawrence, A. L. Cornelius, and J. J. Neumeier, Phys. Rev. B **57**, 10440 (1998).

[76] T. Arima, Y. Tokura, and J. B. Torrance, Phys. Rev. B **48**, 17006 (1993).

[77] J. H. Jung, K. H. Kim, D. J. Eom, T. W. Noh, E. J. Choi, J. Yu, Y. S. Kwon, and Y. Chung, Phys. Rev. B **55**, 15489 (1997).

[78] E. S. Bozin, M. Schmidt, A. J. DeConinck, G. Paglia, J. F. Mitchell, T. Chatterji, P. G. Radaelli, T. Proffen, and S. J. L. Billinge, Phys. Rev. Lett. **98**, 137203 (2007).

[79] E. O. Wollan and W. C. Koehler, Phys. Rev. **100**, 545 (1955).

[80] J. Y. T. Wei, N. C. Yeh, R. P. Vasquez, and A. Gupta, J. Appl. Phys. **83**, 7366 (1998).